Unlocking the Potential of 2D WTe₂/ZrS₂ van der Waals Heterostructures for Tunnel Field-Effect Transistors:

CHEMISTRY OF MATERIALS

Open Access

pubs.acs.org/cm

Article

Unlocking the Potential of 2D WTe_2/ZrS_2 van der Waals Heterostructures for Tunnel Field-Effect Transistors: Broken-Gap Band Alignment and Electric Field Effects

Konstantina Iordanidou,* Samuel Lara-Avila, Sergey Kubatkin, Saroj P. Dash, and Julia Wiktor

Cite This: *Chem. Mater.* 2024, 36, 11317−11325

Read Online

ACCESS | Metrics & More | Article Recommendations | Supporting Information

ABSTRACT: Heterostructures composed of two-dimensional materials open new avenues for advancing semiconductor technology, particularly in the development of energy-efficient tunnel field effect transistors (TFETs). Here, we employ density functional theory calculations to investigate the electronic behavior of WTe_2/ZrS_2 heterostructures having diverse dimensions and arrangement motifs. Our simulations suggest that the topmost valence band of WTe_2 overlaps with the bottommost conduction band of ZrS_2, giving rise to the broken gap or type-III band alignment, which is favorable for fabricating TFETs. Using first-principles molecular dynamics simulations, the temperature effect on the electronic properties is studied, demonstrating that the broken gap band alignment is preserved at 300 K. Furthermore, the electronic properties of the heterostructures are shown to be affected by external electric fields: positive electric fields increase the overlap between the valence and conduction states, whereas negative electric fields lead to the opposite effect. Interestingly, a Rashba-type spin splitting is observed in the topmost valence band, and the Rashba energy is slightly influenced by the presence of external electric fields. Overall, our study sheds light on the inherent characteristics of WTe_2/ZrS_2 heterostructures and can be valuable for fabricating TFETs with optimal performance.

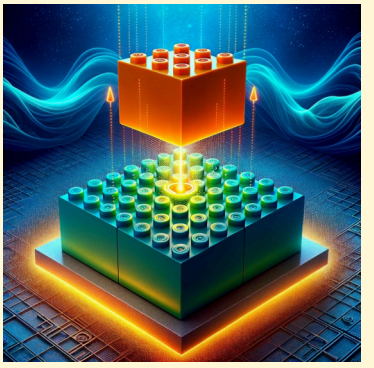

1. INTRODUCTION

In recent decades, technological progress has led to the creation of smaller transistors and devices incorporating billions of them on a single chip. However, as the dimensions of transistors are reduced, energy consumption and heat production become critical concerns for continued progress. In the quest to decrease energy consumption, a major challenge is achieving efficient switching between the on and off states. This is characterized by the subthreshold swing (SS) which is limited to SS > 60 mV/dec at T = 300 K, known as the thermionic limit. To circumvent this fundamental limit, alternative transistor designs have been developed, like the tunnel field-effect transistors (TFETs).[1−3] TFETs rely on quantum mechanical tunneling phenomena and exploit the band-to-band tunneling of charge carriers. When properly designed, the tunneling effect can be extremely sensitive to the gate voltage, leading to an SS < 60 mV/dec Given the need for tight electrostatic control of materials and interfaces for high-performance devices, two-dimensional (2D) van der Waals (vdW) heterostructures hold high potential for next-generation TFETs.[4−6] Their atomically sharp interfacial regions suppress the trap-assisted tunneling, and low screening in 2D materials suggests that their band alignments are easily controlled by external electric fields (i.e., the gate voltage).

Two-dimensional transition metal dichalcogenides (TMDs) and their van der Waals heterostructures[7−24] have been extensively examined for next-generation nanoelectronics. Two-dimensional ZrS_2 has been experimentally realized through the electrochemical lithiation technique,[25] whereas large-area and uniform films have been additionally developed by atomic layer deposition.[26] Theoretical studies suggest that the phonon limited electron mobility of 2D ZrS_2 is 1247 $cm^2\ V^{-1}\ s^{-1}$ at T = 300 K,[27] i.e., larger than the corresponding values of other well-studied TMDs like MoS_2. Through first-principles simulations, heterostructures composed of 2D ZrS_2 have been explored and found promising for various applications such as optoelectronics,[28] solar energy conversion,[29] and photocatalytic water splitting.[30−32] Another appealing member of the TMD family is 2D WTe_2, and nanosheets of the hexagonal phase (H-WTe_2) have been recently synthesized via a lithium-intercalation-assisted technique.[33]

Experimentally, the fabrication of van der Waals heterostructures, like WTe_2/ZrS_2, is feasible through well-established methods. A common technique is mechanical exfoliation followed by deterministic stacking using a dry-transfer process, which allows for precise control over the alignment and stacking of individual monolayers. Additionally, chemical vapor deposition and atomic layer deposition are being used to grow large-

Received: October 1, 2024
Revised: October 21, 2024
Accepted: October 22, 2024
Published: November 13, 2024

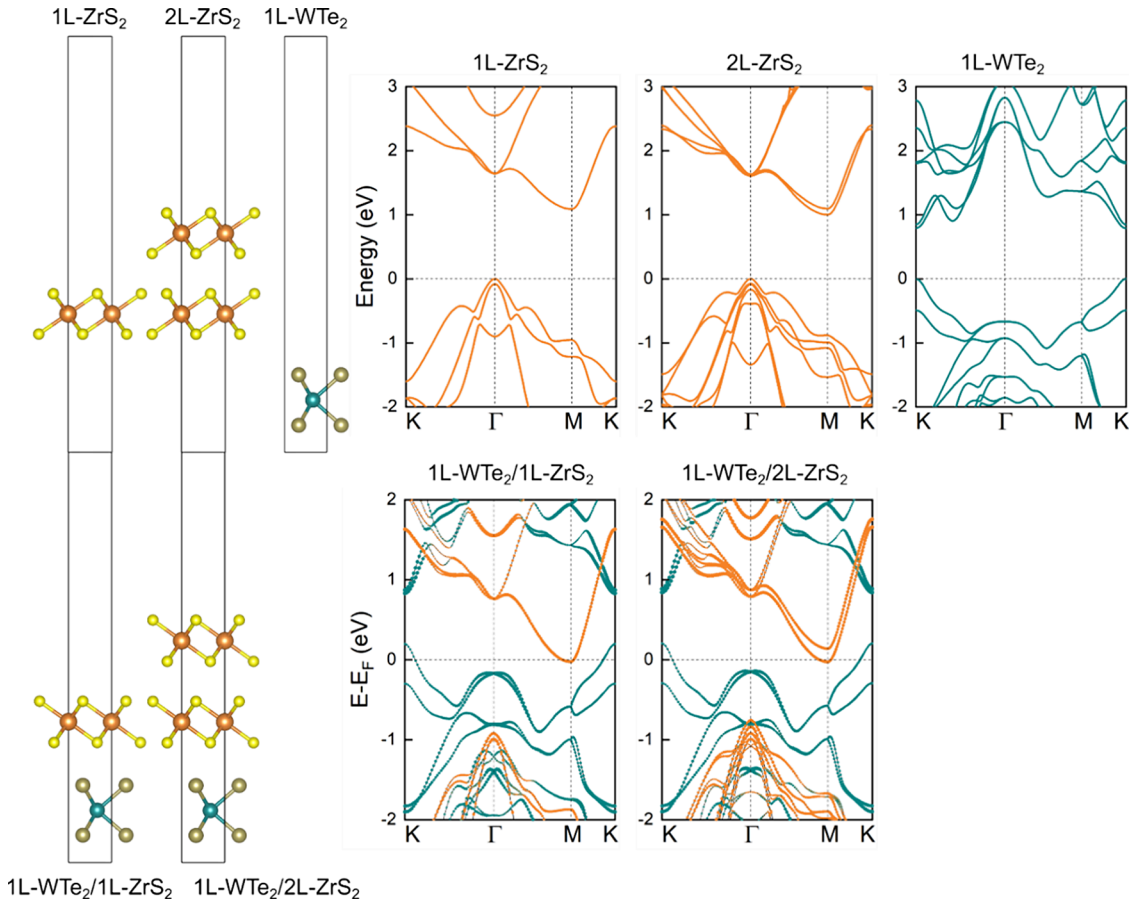

Figure 1. Optimized models of monolayer ZrS_2 (1L-ZrS_2), bilayer ZrS_2 (2L-ZrS_2), monolayer WTe_2 (1L-WTe_2), and their most stable heterostructures (1L-WTe_2/1L-ZrS_2 and 1L-WTe_2/2L-ZrS_2) along with their electronic band structures. Green and orange spheres indicate W and Zr metal atoms, whereas brown and yellow spheres indicate Te and S chalcogen atoms, respectively. For the band structures of the isolated systems namely 1L-ZrS_2, 2L-ZrS_2, and 1L-WTe_2 the energies are referenced to the valence band maximum. For the band structures of the heterostructures, the green and orange lines indicate the contributions to the electronic states from WTe_2 and ZrS_2, respectively. For all band structure calculations spin−orbit coupling is considered.

area monolayers and heterostructures with minimal defects. Twist angle control in such heterostructures can be achieved with manual rotation during the stacking process, providing flexibility to explore various stacking configurations.

In general, excitons, which are bound electron−hole pairs, play a significant role in the optical and electronic properties of 2D materials due to the reduced dielectric screening and enhanced Coulomb interactions in such systems. In heterostructures with a broken-gap band alignment, exciton formation at the interface can be enhanced, particularly under optical excitation. This occurs because the electron and hole can reside in different layers, leading to the formation of spatially indirect excitons. These interlayer excitons are expected to exhibit long lifetimes due to spatial separation, which can be advantageous for applications in optoelectronic devices, such as photodetectors and excitonic transistors. Additionally, the interaction of excitons with the band alignment may influence the tunneling behavior in TFETs. The energy landscape created by the broken-gap alignment could facilitate efficient exciton dissociation, with the resulting free carriers contributing to the tunneling current.

In our work, we deploy density functional theory (DFT) to explore the electronic behavior of WTe_2/ZrS_2 heterostructures, featuring various dimensions and layer distribution patterns. Our simulations show that the studied heterostructures exhibit the type-III band alignment which facilitates efficient tunneling of charge carriers. Furthermore, we find that external electric fields can affect the electronic properties of the heterostructures: positive fields increase the valence and conduction bands overlap, whereas negative fields have the opposite effect.

2. MODELS AND COMPUTATIONAL METHODS

Our first-principles calculations are carried out using the Vienna Ab initio Simulation Package (VASP),[34,35] and for the electron−ion interaction, we use the projector augmented wave (PAW) potentials.[36] van der Waals heterostructures with low deformation are produced by the Cellmatch code.[37] We apply periodic boundary conditions, and we add a vacuum region perpendicular to the plane of the interface. van der Waals corrections are incorporated during relaxations and total energy evaluations, using the rev-vdW-DF2 functional.[38] For all other computations, the Perdew−Burke−Ernzerhof (PBE) functional is employed.[39] Our models are relaxed through the conjugate gradient method with force and energy thresholds of 0.01 eV/Å and 10^{-8} eV, respectively. An energy cutoff of 500 eV is selected for the plane-wave expansion. We employ a 16 × 16 × 1 k-mesh for the relaxations of heterostructures composed of WTe_2 and ZrS_2 unit cells, whereas a 4 × 4 × 1 k-mesh is used for the relaxations of heterostructures with low deformation. Denser k-meshes are adopted for the electronic structure calculations. For computations involving external electric fields, dipole corrections are applied vertically to the interface.

Relativistic effects on the electronic properties are also explored. Based on the rev-vdW-DF2 relaxed structures, spin−orbit coupling is

https://doi.org/10.1021/acs.chemmater.4c02738
Chem. Mater. 2024, 36, 11317−11325

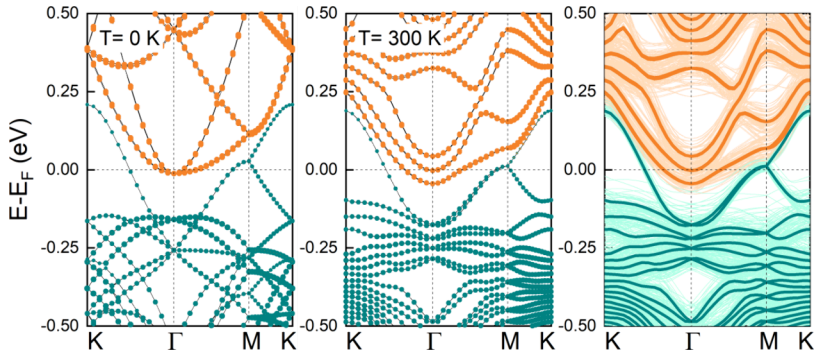

Figure 2. Electronic band structures of the favorable $(1 \times 1)WTe_2/(1 \times 1)ZrS_2$ heterostructure (considering a $4 \times 4 \times 1$ supercell) at different temperatures. The left panel displays the band structure at 0 K. The middle panel shows the averaged band structure at 300 K, representing thermal effects on the electronic states. The right panel provides the band structures from all snapshots considered at 300 K (along with the averaged band structure at 300 K), highlighting the distribution and variance in electronic states due to thermal fluctuations. The green and orange lines indicate the contributions to the electronic states from WTe_2 and ZrS_2, respectively. For all band structure calculations spin−orbit coupling is considered.

activated, and band structure calculations are performed through the PBE functional, consistent with the approach adopted in other reports.[40] To verify the reliability of our approach, we performed additional calculations using the vdW-DF-cx functional which supports SOC.[41] First, we relaxed the heterostructures using vdW-DF-cx, and then we computed the band structures using both vdW-DF-cx with SOC and PBE with SOC. Interestingly, the computed band structures are nearly identical, reinforcing the reliability of our approach. To mitigate the shortcomings in precisely predicting band gaps by DFT, the HSE06 hybrid functional is employed.[42] To evaluate the temperature effect on the electronic properties, we carry out first-principles molecular dynamics (MD) considering a $4 \times 4 \times 1$ supercell and using the same parametrization scheme as the 0 K simulations. We employ the canonical NVT ensemble at 300 K and we adopt the Nose-Hoover thermostat for the temperature control.[43,44] Our MD simulations are carried out for 10 ps using a time step of 2 fs, where the first 1 ps is considered as equilibration and we only use the last 9 ps for statistics.

3. RESULTS AND DISCUSSION

3.1. Inherent Characteristics of WTe_2/ZrS_2 Heterostructures. WTe_2 and ZrS_2 monolayers are composed of one hexagonal plane of metal atoms (W or Zr), sandwiched between two hexagonal planes of chalcogen atoms (Te or S). For our study, WTe_2 (ZrS_2) exhibits the trigonal prismatic (octahedral) coordination with relaxed lattice parameters of 3.533 (3.659) Å in the monolayer regime, in good agreement with previously reported simulations.[45,46] The in-plane lattice mismatch is below 4.0%, and first, we build $(1 \times 1)WTe_2/(1 \times 1)ZrS_2$ heterobilayers by placing their respective unit cells on top of each other. For our models, the total strain is shared within the layers, i.e., the WTe_2 lattice is elongated by ∼2% whereas the ZrS_2 lattice is shortened by this amount. During the optimization process, the atomic positions are adjusted while keeping the lattice parameters unchanged. It is worth noting that test calculations where both the atomic positions and the lattice parameters are optimized are also performed, and nearly no differences are observed in the structural and electronic properties of the heterostructures. By changing the relative positions of the layers, we consider heterobilayers with six high-symmetry layer distribution patterns herein referred to as vdWH-I, vdWH-II, vdWH-III, vdWH-IV, vdWH-V, and vdWH-VI (see Supporting Information, Figure S1). We find that vdWH-IV, for which top-layer S atoms are located above Te atoms and bottom-layer S atoms lie above W atoms, corresponds to the lowest energy stack. Interestingly, vdWH-II has only 0.4 meV/atom larger energy compared to vdWH-IV. Concerning the structural characteristics, considering the most stable stack, the interlayer distance defined as the separation between the upper-layer Te atoms and the lower-layer S atoms is found to be 3.1 Å, whereas for the rest of the stacks, it spans from 3.1 to 3.7 Å (see Supporting Information, Table SI).

As a next step, we calculate the binding energies of the heterostructures through the relation

$$E_b = E_{tot}(WTe_2/ZrS_2) - E_{tot}(WTe_2) - E_{tot}(ZrS_2) \quad (1)$$

where the three terms $E_{tot}(WTe_2/ZrS_2)$, $E_{tot}(WTe_2)$, and $E_{tot}(ZrS_2)$ correspond to the total energies of the heterobilayer, the isolated stretched WTe_2 monolayer, and the isolated compressed ZrS_2 monolayer. Considering the most stable stack E_b is −23 meV/Å^2, and for the rest of the stacks the binding energies span from −23 to −15 meV/Å (see Supporting Information, Table SI). Note that the negative binding energies imply thermodynamically stable structures that can be experimentally synthesized.

Concerning the electronic behavior, our PBE calculations with SOC suggest that WTe_2 and ZrS_2 monolayers are semiconductors with band gaps of 0.79 and 1.09 eV, respectively, and our results are in good agreement with other theoretical calculations.[47] The band structure of the most stable stack is shown in Figure 1 and comparable band structures are found for the rest of the stacks (see Supporting Information, Figures S2 and S3). Interestingly, we observe that the upermost valence band (VB) originating from WTe_2, overlaps with the lowermost conduction band (CB) originating from ZrS_2, giving rise to the broken gap or type-III band alignment which is favorable for fabricating TFETs. The energy difference between the conduction and valence band edges is $\Delta E_{CBM-VBM} = -0.22$ eV. Without SOC, WTe_2 and ZrS_2 band gaps slightly increase by 0.33 and 0.03 eV, respectively, whereas for their heterostack we find $\Delta E_{CBM-VBM} = -0.08$ eV. To mitigate the shortcomings in precisely predicting band gaps by DFT, hybrid functional calculations are additionally carried out (see Supporting Information, Figure S4). Focusing on the lowest energy heterobilayer, our HSE06 calculations without SOC revealed that the energy difference between the conduction and valence band edges is −0.12 eV. Using HSE06 with SOC the energy difference is −0.16 eV, i.e., the inclusion of SOC further increases the overlap by about 0.04 eV (see Supporting Information, Figure S5). Overall, we concluded that although the band gaps of isolated WTe_2 and ZrS_2 monolayers are

https://doi.org/10.1021/acs.chemmater.4c02738
Chem. Mater. 2024, 36, 11317−11325

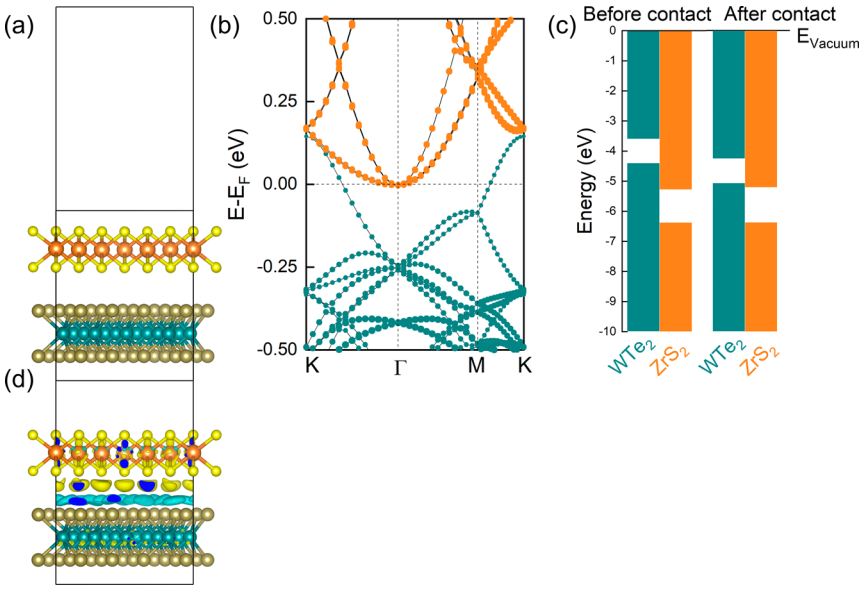

Figure 3. (a, b) Optimized model of $(\sqrt{13} \times \sqrt{13})WTe_2/(\sqrt{12} \times \sqrt{12})ZrS_2$ heterostructure with low deformation along with its electronic band structure, (c) band alignments relative to the vacuum level prior to and after stacking, and (d) charge density difference computed by $\Delta\rho_c = \rho(WTe_2/ZrS_2) - \rho(WTe_2) - \rho(ZrS_2)$. The green and orange lines indicate the contributions to the electronic states from WTe_2 and ZrS_2, respectively. Blue and yellow isosurfaces indicate electron depletion and accumulation, respectively, and an isosurface value of 0.0005 electrons/Bohr^3 is selected. Spin−orbit coupling is considered in the computations.

increased in hybrid functional calculations, the broken gap band alignment of the heterostructure is preserved.

The value of the broken gap is relatively small, particularly compared to the band gap renormalization at room temperature expected for TMDs.[48] Therefore, to assess how thermal disorders affect the band alignment of WTe_2/ZrS_2 heterostructures, we carry out MD simulations at 300 K. From the MD trajectory, we extract 46 evenly spaced snapshots, and we calculate their band structure using PBE with SOC. Figure 2 shows the averaged band structure, along with the distribution of the band structures from all considered snapshots. For the sake of comparison, the band structure obtained by considering fixed atomic positions at 0 K is also shown. We observe that the band alignment is not largely affected by the temperature and the broken gap of −0.23 eV is retained at 300 K. However, the dispersion of particular electron states changes with temperature, and most notably, the uppermost valence band at Γ-point exhibits significant fluctuations with temperature, where the instantaneous energy of this band can differ by up to ∼0.1 eV from the average value. We also examine the atomic displacements during the MD simulations by calculating the radial distribution functions (RDFs, see Supporting Information, Figure S7). We note that the temperature only results in fluctuations in the bond lengths, while the average distances between the atoms are retained (with first peaks in the RDFs agreeing well with bond lengths at 0 K, 2.74 Å for W−Te and 2.55 Å for Zr−S bonds). The widths of the first peaks in the RDF suggest fluctuations of distances between the first neighbors of about 0.2 Å for W−Te and 0.4 Å for Zr−S as compared to the 0 K values, in agreement with the smaller atomic mass of S.

For the studied heterobilayers, besides the broken-gap band alignment, a Rashba-type spin splitting is observed in the vicinity of the Γ-point, which can be particularly promising for spintronic applications (see Supporting Information, Figure S8). When ZrS_2 is placed above WTe_2 to form the heterostructure, the out-of-plane symmetry of single-layer WTe_2 is disrupted, leading to the observation of the Rashba effect. In the KΓ direction, the maximum momentum offset and the energy difference between the band extremum and the band degenerate Γ-point are k_R = 0.07 Å^{-1} and E_R= 8 meV, respectively. It is worth noting that the Rashba splitting is rather small in these systems and considering the effect of temperature on the band structure, one can expect it to be mostly prominent at low temperatures.[49]

Next, to evaluate the transport behavior, the electron effective masses are computed using the relation $1/m^* = \partial^2 E(k)/(\hbar^2 \partial k^2)$ where $\hbar$ refers to the reduced Planck constant. For the isolated (nondeformed) single-layer WTe_2, the effective masses in the ΓK and MK directions are 0.38 and 0.42 m_o, whereas for ZrS_2 the corresponding values in the ΓM and KM directions are 1.99 and 0.30 m_o. For the most stable stack, we find $m_{e,\Gamma M}$ = 1.81 m_o and $m_{e,KM}$ = 0.27 m_o and similar results are observed in the rest of the stacks (see Supporting Information, Table SI). Overall, our findings reveal highly anisotropic electronic behavior where the light masses along the KM direction indicate high mobility contrary to the heavy masses along the ΓM direction.[50]

Considering that the work function of WTe_2 is smaller than that of ZrS_2,[47] electrons instinctively migrate from WTe_2 to ZrS_2 upon stacking. Our charge analysis using the Bader formalism (performed through the PBE functional with SOC) shows that approximately 5 × 10^{13} e/cm^2 move from WTe_2 to ZrS_2 for vdWH-IV. For calculating the charge density differences, we use the relation:

$$\Delta\rho_c = \rho(WTe_2/ZrS_2) - \rho(WTe_2) - \rho(ZrS_2)$$

where the three terms $\rho(WTe_2/ZrS_2)$, $\rho(WTe_2)$ and $\rho(ZrS_2)$ correspond to the charge density of the heterobilayer, the isolated WTe_2 monolayer and the isolated ZrS_2 monolayer, respectively (see Supporting Information, Figure S9). As anticipated, the top-layer chalcogen atoms of WTe_2 and the bottom-layer chalcogen atoms of SnS_2 primarily contribute to the charge exchange. Consistent with our charge analysis, we

https://doi.org/10.1021/acs.chemmater.4c02738
Chem. Mater. 2024, 36, 11317−11325

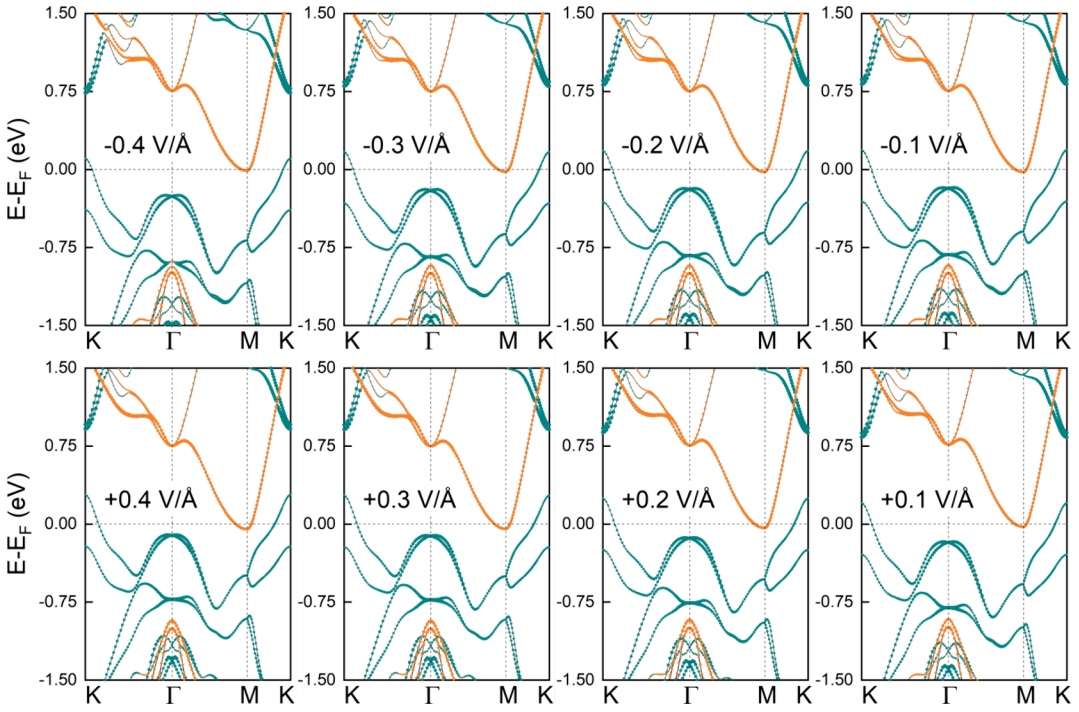

Figure 4. Band structures of the favorable $(1 \times 1)WTe_2/(1 \times 1)ZrS_2$ heterostructure upon electric field application. The green and orange lines indicate the contributions to the electronic states from WTe_2 and ZrS_2, respectively. Spin−orbit coupling is considered in the computations.

find that WTe_2 depletes electrons whereas ZrS_2 accumulates electrons, and the heterostack looks like a miniaturized capacitor of parallel plates with an inherent electric field pointing to ZrS_2.

In experiments, heterobilayers having different twist angles between the constituent monolayers are achievable. By varying the twist angle, we look for stacks with low deformation (less than 1%) and a minimal number of atoms (less than 100). Our considered configuration is composed of $(\sqrt{13} \times \sqrt{13})WTe_2$ and $(\sqrt{12} \times \sqrt{12})ZrS_2$ monolayers with a relative twist of 16°. The strain is solely distributed to ZrS_2, and various translation operations are applied. We systematically displace ZrS_2 relative to WTe_2 in the a/b directions by $0.2a$ and/or $0.2b$, and for each displaced configuration we perform atomic optimizations. Interestingly, we find that the energy landscape is relatively flat and the energy difference between the most and least stable structures is just 0.01 meV/atom, whereas a negative binding energy of −18 meV/Å^2 is computed. Concerning the electronic behavior, Figure 3 shows the band structure of the heterobilayer with low deformation and the corresponding band alignments prior to and after stacking. Note that the band alignment prior to stacking refers to the isolated nondeformed unit cells. In agreement with our previous findings, WTe_2/ZrS_2 heterobilayers with twisted layers exhibit the type-III band alignment. Through PBE calculations with SOC the energy difference between the conduction and valence band edges is −0.15 eV. Regarding the electron transfer, our charge analysis using the Bader formalism shows that 3×10^{13} e/cm^2 move from WTe_2 to ZrS_2 upon stacking.

Furthermore, we examine thicker heterostructures composed of monolayer WTe_2 and bilayer (2L), trilayer (3L), tetralayer (4L), or pentalayer (5L) ZrS_2. For few-layer ZrS_2, we consider the most stable structure where the layers are stacked on one another with no shifts or rotations.[51] The relaxed lattice constants are very similar to those of single-layer, namely $a_{ZrS_2,2L} = a_{ZrS_2,3L} = a_{ZrS_2,4L} = 3.655$ Å and $a_{ZrS_2,5L} = 3.654$ Å. Owing to the low lattice mismatch between WTe_2 and ZrS_2, we build heterostructures by placing their respective unit cells on top of each other and by sharing the strain within the layers. Initially, heterostructures composed of WTe_2 monolayers and ZrS_2 bilayers are discussed. By changing the relative positions of the layers, we consider configurations with six high symmetry layer distribution patterns herein referred to as vdWH-3L-I, vdWH-3L-II, vdWH-3L-III, vdWH-3L-IV, vdWH-3L-V, and vdWH-3L-VI (see Supporting Information, Figure S10). We find that vdWH-3L-IV, for which top-layer S atoms are located above Te atoms and bottom-layer S atoms lie above W atoms, corresponds to the lowest energy stack. Interestingly, vdWH-3L-II has only 0.3 meV/atom larger energy compared to vdWH-3L-IV, and these results are in agreement with our findings for WTe_2/ZrS_2 heterobilayers. Our PBE calculations with SOC suggest that ZrS_2 bilayer has a band gap of 1.00 eV, i.e., slightly smaller compared to the single-layer system. The band structure of the most stable heterostructure is shown in Figure 1, and similar band structures are found for the rest of the heterostructures (see Supporting Information, Figures S11 and S12). Interestingly, the broken-gap band alignment and the Rashba type spin splitting of the uppermost valence band are also observed in this system. Using PBE with SOC, the energy difference between the conduction and valence band edges is −0.23 eV, i.e., nearly the same as the corresponding value of the WTe_2/ZrS_2 heterobilayer. Next, heterostructures composed of single-layer WTe_2 and trilayer/tetralayer/pentalayer ZrS_2 are discussed. For our investigation, we consider only one configuration of high symmetry, which is structurally equivalent to the energetically favorable configurations of 1L-WTe_2/1L-ZrS_2 and 1L-WTe_2/2L-ZrS_2 heterostructures (meaning the top-layer S atoms are located above Te atoms and the bottom-layer S atoms lie above W atoms, see Supporting Information, Figure S13). Our PBE calculations with SOC suggest that the trilayers, tetralayers, and pentalayers of ZrS_2 have band gaps of 0.96, 0.95,

https://doi.org/10.1021/acs.chemmater.4c02738
Chem. Mater. 2024, 36, 11317−11325

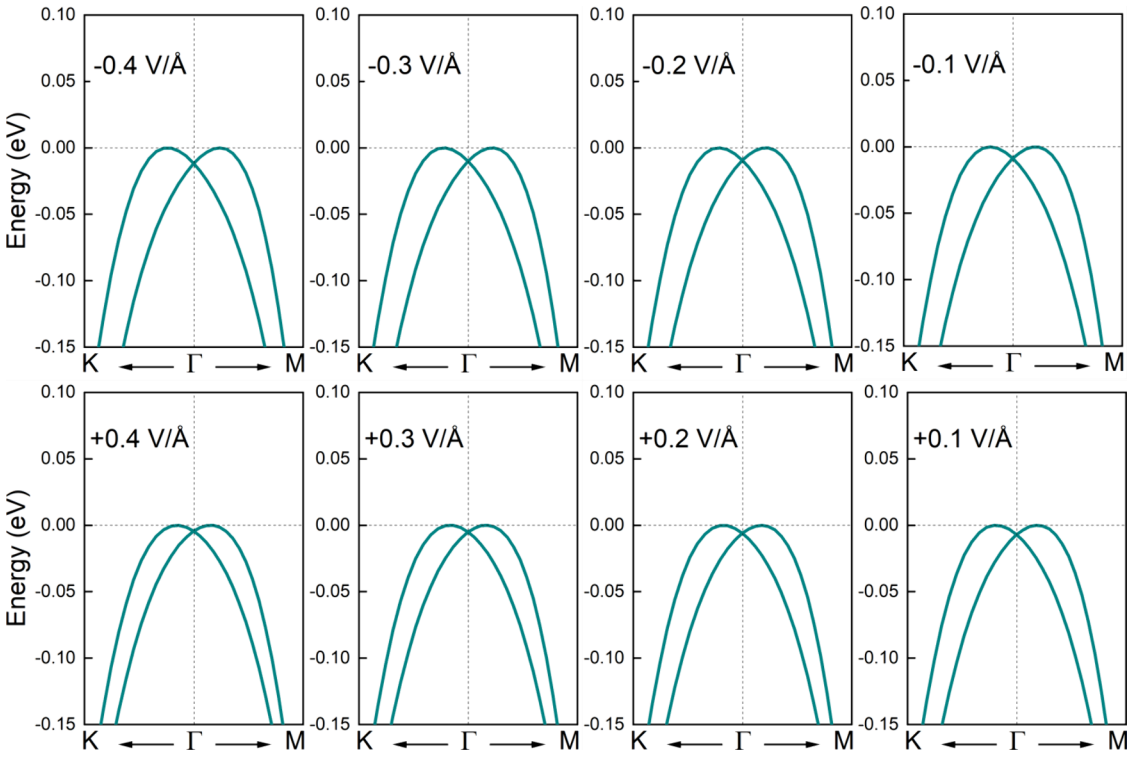

Figure 5. Zoomed-in view of the band structures of the favorable $(1 \times 1)WTe_2/(1 \times 1)ZrS_2$ heterostructure upon electric field application, showing the Rashba-type spin splitting.

and 0.90 eV, respectively. Interestingly, the broken-gap band alignment and the Rashba-type spin splitting of the uppermost valence band are observed in these thicker systems (see Supporting Information, Figure S14) and the energy differences between the conduction and valence band edges are about −0.23 eV.

Lastly, we examine thicker heterostructures composed of monolayer ZrS_2 and bilayer (2L), trilayer (3L), and tetralayer (4L) WTe_2. The relaxed lattice constants of few-layer WTe_2 are very similar to those of single-layer WTe_2, namely $a_{WTe_2,2L} = 3.534$ Å and $a_{WTe_2,3L} = a_{WTe_2,4L} = 3.535$ Å. First, heterostructures composed of ZrS_2 monolayers and WTe_2 bilayers are addressed. By changing the relative positions of the layers, we consider configurations with six high symmetry layer distribution patterns herein referred to as vdWH-3L'-I, vdWH-3L'-II, vdWH-3L'-III, vdWH-3L'-IV, vdWH-3L'-V, and vdWH-3L'-VI (see Supporting Information, Figure S15). We find that vdWH-3L'-II, for which top-layer S atoms are located above Te atoms and bottom-layer S atoms lie above W atoms of the WTe_2 layer at the interface, corresponds to the lowest energy stack. Notably, the broken-gap band alignment is observed in these systems (see Supporting Information, Figures S16 and S17), and for the energetically favorable heterostructure, using PBE with SOC the energy difference between the conduction and valence band edges is −0.17 eV. Next, heterostructures composed of ZrS_2 monolayers and WTe_2 trilayers or tetralayers are addressed, and only one configuration of high symmetry is considered (see Supporting Information, Figure S18). This configuration is equivalent to the energetically favorable structure observed upon stacking single-layer ZrS_2 and single-layer or bilayer WTe_2. Concerning the electronic properties, the thicker heterostructures exhibit the broken gap band alignment similar to their thinner counterparts (see Supporting Information, Figure S19). Overall, our simulations suggest that heterostructures of WTe_2 and ZrS_2 with diverse dimensions and arrangement motifs present the type-III band alignment which holds high potential for fabricating TFETs.

3.2. Harnessing External Electric Fields. Next, we explore the effects of external electric fields (E_{ext}) on the electronic properties of $(1 \times 1)WTe_2/(1 \times 1)ZrS_2$ heterobilayers. E_{ext} is imposed vertically to the interface and positive values correspond to fields pointing to ZrS_2. For our study, E_{ext} spans from −0.4 to 0.4 V/Å with steps of 0.1 V/Å. The electric field is considered not only in the electronic structure calculations but also in the atomic optimizations. Owing to the applied electric field, a potential gradient perpendicular to the interface is induced, which leads to the charge carrier redistribution. The positions of the band edges are affected by the redistribution of the carriers, and Figure 4 presents the band structures of the heterobilayers in the presence of E_{ext}.

We find that for positive electric fields, WTe_2 VB edge positions move upwardly relative to the Fermi level, contrary to ZrS_2 CB edge positions. As the positive electric fields are intensified, the shifts in the band edges become more pronounced. Performing PBE calculations with SOC, by modifying the electric field from 0.2 to 0.4 V/Å the difference in energy between the VB and CB edges alters from −0.28 to −0.33 eV. Smaller energy differences correspond to larger overlaps between the valence and conduction states, implying larger electron tunneling from WTe_2 to ZrS_2. A reverse response is found for $E_{ext} < 0$, and although the overlap between the valence and conduction states decreases, the type-III band alignment is preserved. PBE calculations without SOC are also conducted and comparable results are observed (see Supporting Information, Figure S20). Furthermore, HSE calculations without SOC are carried out and the trends are similar to those of PBE (see Supporting Information, Figure S21). As

https://doi.org/10.1021/acs.chemmater.4c02738
Chem. Mater. 2024, 36, 11317−11325

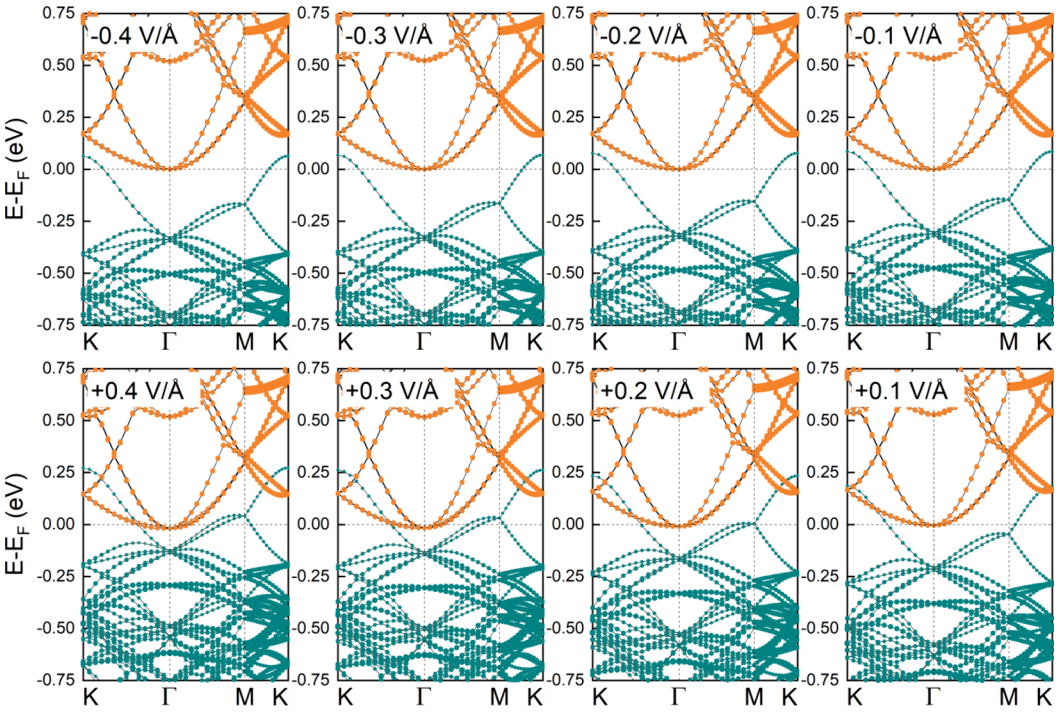

Figure 6. Band structures of $(\sqrt{13} \times \sqrt{13})WTe_2/(\sqrt{12} \times \sqrt{12})ZrS_2$ heterostructure with low deformation upon electric field application. The green and orange lines indicate the contributions to the electronic states from WTe_2 and ZrS_2, respectively. Spin−orbit coupling is considered in the computations.

shown in Figure 5, for negative electric fields both the Rashba energy (E_R) and the wavenumber difference (k_R) are marginally enhanced. For instance, by modifying the electric field from 0 to −0.4 V/Å, E_R goes from 8 to 12 meV and k_R goes from 0.07 to 0.09 Å^{-1}.

As shown in Figure 6, simulations considering electric fields are also carried out for heterobilayers having twisted layers. Consistent with our earlier findings, $E_{ext} > 0$ leads to larger overlaps between the VB and CB states, contrary to our results for $E_{ext} < 0$. Performing PBE calculations with SOC, by modifying the electric field from 0.2 to 0.4 V/Å the energy difference between the CB and VB edges alters from −0.25 to −0.29 eV. PBE calculations without SOC are also conducted and comparable results are observed (see Supporting Information, Figure S22). Note that when SOC is neglected, a transition from the type-III to the type-II band alignment is induced for $E_{ext} < 0$. Also note that for $(\sqrt{13} \times \sqrt{13})WTe_2/(\sqrt{12} \times \sqrt{12})ZrS_2$ heterobilayer, the separation between the upper-layer Te atoms and the lower-layer S atoms is 3.4 Å, and a 0.4 V/Å electric field refers to a 1.4 V potential difference. Similarly, for $(1 \times 1)WTe_2/(1 \times 1)ZrS_2$ heterobilayer the interlayer distance is 3.1 Å and E_{ext} = 0.4 V/Å refers to ΔV = 1.2 V.

4. CONCLUSIONS

In this work, through first-principles density functional theory calculations, we explored the inherent characteristics of stacks consisting of WTe_2 and ZrS_2. We found that WTe_2/ZrS_2 heterostructures with diverse dimensions and arrangement motifs exhibit the type-III or broken gap band alignment which holds high potential for fabricating TFETs. Our charge analysis using the Bader formalism showed that electrons instinctively migrate from WTe_2 to ZrS_2 upon stacking and the heterostructures look like miniaturized capacitors of parallel plates with inherent electric fields pointing to ZrS_2. First-principles molecular dynamics simulations were also performed, and we found that the type-III band alignment is preserved at 300 K. Furthermore, we examined the impact of electric fields on the electronic properties. By enhancing the positive electric fields, the overlap between the high-lying valence states of WTe_2 and the low-lying conduction states of ZrS_2 is enhanced, implying larger tunneling currents. Interestingly, besides the broken gap band alignment, a Rashba-type spin splitting was observed in WTe_2/ZrS_2 heterostructures, owing to the out-of-plane symmetry break.

■ ASSOCIATED CONTENT

Supporting Information

The Supporting Information is available free of charge at https://pubs.acs.org/doi/10.1021/acs.chemmater.4c02738.

Optimized $(1 \times 1)WTe_2/(1 \times 1)ZrS_2$ heterobilayers and their band structures with/without SOC; structural/electronic properties and binding energies of $(1 \times 1)WTe_2/(1 \times 1)ZrS_2$ heterobilayers; HSE06 band structures of $(1 \times 1)WTe_2/(1 \times 1)ZrS_2$ heterobilayers without SOC; HSE06 band structures of the most favorable $(1 \times 1)WTe_2/(1 \times 1)ZrS_2$ heterobilayer with/without SOC; snapshots of MD simulations; radial distribution functions; zoomed-in view of band structures of $(1 \times 1)WTe_2/(1 \times 1)ZrS_2$ heterobilayers with SOC; charge density differences of $(1 \times 1)WTe_2/(1 \times 1)ZrS_2$ heterobilayers; optimized stacks composed of monolayer WTe_2 and bilayer ZrS_2 and their band structures with/without SOC; optimized stacks composed of monolayer WTe_2 and tri-, tetra-, penta-layer ZrS_2 and their band structures with/without SOC; optimized stacks composed of monolayer ZrS_2 and bilayer WTe_2 and their band structures with/without SOC; optimized stacks com-

https://doi.org/10.1021/acs.chemmater.4c02738
Chem. Mater. 2024, 36, 11317−11325

posed of monolayer ZrS_2 and tri-, tetra-layer WTe_2 and their band structures with/without SOC; band structures of the most favorable $(1 \times 1)WTe_2/(1 \times 1)ZrS_2$ heterobilayer in the presence of external electric fields without SOC; HSE06 band structures of the most favorable $(1 \times 1)WTe_2/(1 \times 1)ZrS_2$ heterobilayer in the presence of external electric fields without SOC; and band structures of $(\sqrt{13} \times \sqrt{13})WTe_2/(\sqrt{12} \times \sqrt{12})ZrS_2$ heterobilayer in the presence of external electric fields without SOC (PDF)

AUTHOR INFORMATION

Corresponding Author

Konstantina Iordanidou − *Materials Physics-Oslo, Department of Sustainable Energy Technology, SINTEF Industry, NO-0314 Oslo, Norway; Department of Physics, Chalmers University of Technology, SE-412 96 Gothenburg, Sweden;* orcid.org/0000-0003-4696-8204; Email: konstantina.iordanidou@sintef.no

Authors

Samuel Lara-Avila − *Department of Microtechnology and Nanoscience, Chalmers University of Technology, SE-412 96 Gothenburg, Sweden; National Physical Laboratory, Teddington TW11 0LW, United Kingdom;* orcid.org/0000-0002-8331-718X

Sergey Kubatkin − *Department of Microtechnology and Nanoscience, Chalmers University of Technology, SE-412 96 Gothenburg, Sweden;* orcid.org/0000-0001-8551-9247

Saroj P. Dash − *Department of Microtechnology and Nanoscience, Chalmers University of Technology, SE-412 96 Gothenburg, Sweden;* orcid.org/0000-0001-7931-4843

Julia Wiktor − *Department of Physics, Chalmers University of Technology, SE-412 96 Gothenburg, Sweden;* orcid.org/0000-0003-3395-1104

Complete contact information is available at: https://pubs.acs.org/10.1021/acs.chemmater.4c02738

Notes

The authors declare no competing financial interest.

ACKNOWLEDGMENTS

This work is financially supported by the Swedish Strategic Research Foundation through a Future Research Leader program (FFL21-0129), the "Area of Advance − Energy", the "Area of Advance − Nano", the "Area of Advance−Materials", the 2D TECH VINNOVA competence Center (ref.2019-00068), and the Gender Initiative for Excellence (Genie). The authors acknowledge access to HPC resources provided by UNINETT Sigma2—the National Infrastructure for High-Performance Computing and Data Storage in Norway under the grant nn9393k. We also acknowledge access to HPC resources provided by the National Academic Infrastructure for Supercomputing in Sweden (NAISS) at NSC, C3SE, and PDC.

REFERENCES

(1) Bernstein, K.; Cavin, R. K.; Porod, W.; Seabaugh, A.; Welser, J. Device and architecture outlook for beyond CMOS switches. *Proc. IEEE* **2010**, *98*, 2169.

(2) Seabaugh, A. C.; Zhang, Q. Low-voltage tunnel transistors for beyond CMOS logic. *Proc. IEEE* **2010**, *98*, 2095.

(3) Ionescu, A. M.; Riel, H. Tunnel field-effect transistors as energy-efficient electronic switches. *Nature* **2011**, *479*, 329.

(4) Iordanidou, K.; Wiktor, J. Two-dimensional $MoTe_2/SnSe_2$ van der Waals heterostructures for tunnel-FET applications. *Phys. Rev. Mater.* **2022**, *6*, No. 084001.

(5) Iordanidou, K.; Mitra, R.; Shetty, N.; Lara-Avila, S.; Dash, S.; Kubatkin, S.; Wiktor, J. Electric field and strain tuning of 2D semiconductor van der Waals heterostructures for tunnel field-effect transistors. *ACS Appl. Mater. Interfaces* **2023**, *15*, 1762.

(6) Balaji, Y.; Smets, Q.; De La Rosa, C. J. L.; Lu, A. K. A.; Chiappe, D.; Agarwal, T.; Lin, D. H.; Huyghebaert, C.; Radu, I.; Mocuta, D.; Groeseneken, G. Tunneling transistors based on $MoS_2/MoTe_2$ van der Waals heterostructures. *IEEE J. Electron Devices Soc.* **2018**, *6*, 1048.

(7) Zhang, Q.; He, W.; Li, L.; Geng, D.; Xu, Z.; Chen, H.; Chen, W.; Hu, W. Oxygen-assisted anisotropic chemical etching of $MoSe_2$ for enhanced phototransistors. *Chem. Mater.* **2022**, *34*, 4212.

(8) Tedstone, A. A.; Lewis, D. J.; O'Brien, P. Synthesis, properties, and applications of transition metal-doped layered transition metal dichalcogenides. *Chem. Mater.* **2016**, *28*, 1965.

(9) Kundu, T.; Pal, B.; Das, B.; Paramanik, R.; Maity, S.; Ghosh, A.; Palit, M.; Kopciuszynski, M.; Barinov, A.; Mahatha, S. K.; Datta, S. Tunable Electron Transport in Defect-Engineered $PdSe_2$. *Chem. Mater.* **2023**, *35*, 5212.

(10) Iordanidou, K.; Houssa, M.; Pourtois, G.; Afanas'ev, V. V.; Stesmans, A. Oxygen and Hydroxyl Adsorption on MS_2 (M= Mo, W, Hf) Monolayers: A First-Principles Molecular Dynamics Study. *Phys. Status Solidi RRL* **2016**, *10*, 787.

(11) Iordanidou, K.; Houssa, M.; Pourtois, G.; Afanas'ev, V. V.; Stesmans, A. Impact of Point Defects and Oxidation on the Electronic Properties of HfS_2 Monolayers. *ECS J. Solid State Sci. Technol.* **2016**, *5*, Q3054.

(12) Kistanov, A. A. Characterization of Monovacancy Defects in Vanadium Diselenide Monolayer: A DFT Study. *Appl. Sci.* **2024**, *14*, 1205.

(13) Maniadaki, A. E.; Kopidakis, G.; Remediakis, I. N. Strain engineering of electronic properties of transition metal dichalcogenide monolayers. *Solid State Commun.* **2016**, *227*, 33.

(14) Davelou, D.; Mathioudakis, C.; Remediakis, I. N.; Kopidakis, G. Adsorption on metallic edges of transition metal dichalcogenides. *Phys. Status Solidi RRL* **2022**, *16*, No. 2100588.

(15) Lim, H.; Yoon, S. I.; Kim, G.; Jang, A. R.; Shin, H. S. Stacking of two-dimensional materials in lateral and vertical directions. *Chem. Mater.* **2014**, *26*, 4891.

(16) Fu, Q.; Wang, X.; Zhou, J.; Xia, J.; Zeng, Q.; Lv, D.; Zhu, C.; Wang, X.; Shen, Y.; Li, X.; Hua, Y.; et al. One-step synthesis of metal/semiconductor heterostructure NbS_2/MoS_2. *Chem. Mater.* **2018**, *30*, 4001.

(17) Li, L.; Long, R.; Prezhdo, O. V. Charge separation and recombination in two-dimensional MoS_2/WS_2: time-domain ab initio modeling. *Chem. Mater.* **2017**, *29*, 2466.

(18) Hamann, D. M.; Bardgett, D.; Bauers, S. R.; Kasel, T. W.; Mroz, A. M.; Hendon, C. H.; Medlin, D. L.; Johnson, D. C. Influence of Nanoarchitecture on Charge Donation and the Electrical-Transport Properties in $[(SnSe)_{1+\delta}][TiSe_2]_q$ Heterostructures. *Chem. Mater.* **2020**, *32*, 5802.

(19) Chen, J.; Zhou, W.; Tang, W.; Tian, B.; Zhao, X.; Xu, H.; Liu, Y.; Geng, D.; Tan, S. J. R.; Fu, W.; Loh, K. P. Lateral epitaxy of atomically sharp WSe_2/WS_2 heterojunctions on silicon dioxide substrates. *Chem. Mater.* **2016**, *28*, 7194.

(20) Fiori, G.; Bonaccorso, F.; Iannaccone, G.; Palacios, T.; Neumaier, D.; Seabaugh, A.; Banerjee, S. K.; Colombo, L. Electronics based on two-dimensional materials. *Nat. Nanotechnol.* **2014**, *9*, 768.

(21) Thiele, S.; Kinberger, W.; Granzner, R.; Fiori, G.; Schwierz, F. The prospects of transition metal dichalcogenides for ultimately scaled CMOS. *Solid-State Electron.* **2018**, *143*, 2.

(22) Iannaccone, G.; Bonaccorso, F.; Colombo, L.; Fiori, G. Quantum engineering of transistors based on 2D materials heterostructures. *Nat. Nanotechnol.* **2018**, *13*, 183.

(23) Houssa, M.; Iordanidou, K.; Dabral, A.; Lu, A.; Pourtois, G.; Afanasiev, V.; Stesmans, A. Contact resistance at MoS_2-based 2D metal/semiconductor lateral heterojunctions. *ACS Appl. Nano Mater.* **2019**, *2*, 760.
(24) Houssa, M.; Iordanidou, K.; Dabral, A.; Lu, A.; Meng, R.; Pourtois, G.; Afanas'ev, V. V.; Stesmans, A. Contact resistance at graphene/MoS_2 lateral heterostructures. *Appl. Phys. Lett.* **2019**, *114*, 163101.
(25) Zeng, Z.; Yin, Z.; Huang, X.; Li, H.; He, Q.; Lu, G.; Boey, F.; Zhang, H. Single-Layer Semiconducting Nanosheets: High-Yield Preparation and Device Fabrication. *Angew. Chem.* **2011**, *123*, 11289.
(26) Mattinen, M.; Popov, G.; Vehkamäki, M.; King, P. J.; Mizohata, K.; Jalkanen, P.; Räisänen, J.; Leskelä, M.; Ritala, M. Atomic layer deposition of emerging 2D semiconductors, HfS_2 and ZrS_2, for optoelectronics. *Chem. Mater.* **2019**, *31*, 5713.
(27) Zhang, W.; Huang, Z.; Zhang, W.; Li, Y. Two-Dimensional Semiconductors with Possible High Room Temperature Mobility. *Nano Res.* **2014**, *7*, 1731.
(28) Shang, J.; Zhang, S.; Wang, Y.; Wen, H.; Wei, Z. Electronic and optical properties of an intrinsic type-I band alignment ZrS_2/SnS_2 van der Waals heterostructure for optoelectronic devices. *Chin. Opt. Lett.* **2019**, *17*, No. 020010.
(29) Si, Y.; Wu, H. Y.; Yang, H. M.; Huang, W. Q.; Yang, K.; Peng, P.; Huang, G. F. Dramatically Enhanced Visible Light Response of Monolayer ZrS_2 via Non-covalent Modification by Double-Ring Tubular B20 Cluster. *Nanoscale Res. Lett.* **2016**, *11*, 495.
(30) Wang, B.; Wang, X.; Wang, P.; Kuang, A.; Zhou, T.; Yuan, H.; Chen, H. Bilayer $MoTe_2/XS_2$ (X= Hf, Sn, Zr) heterostructures with efficient carrier separation and light absorption for photocatalytic water splitting into hydrogen. *Appl. Surf. Sci.* **2021**, *544*, No. 148842.
(31) Ge, C.; Wang, B.; Yang, H.; Feng, Q.; Huang, S.; Zu, X.; Li, L.; Deng, H. Direct Z-scheme GaSe/ZrS_2 heterojunction for overall water splitting. *Int. J. Hydrogen Energy* **2023**, *48*, 13460.
(32) Wang, G.; Chang, J.; Guo, S. D.; Wu, W.; Tang, W.; Guo, H.; Dang, S.; Wang, R.; Ang, Y. S. MoSSe/Hf(Zr)S_2 heterostructures used for efficient Z-scheme photocatalytic water-splitting. *Phys. Chem. Chem. Phys.* **2022**, *24*, 25287.
(33) Li, S.; Lei, F. C.; Peng, X.; Wang, R. Q.; Xie, J. F.; Wu, Y. P.; Li, D. S. Synthesis of semiconducting 2H-phase WTe_2 nanosheets with large positive magnetoresistance. *Inorg. Chem.* **2020**, *59*, 11935.
(34) Kresse, G.; Furthmüller, J. Efficient Iterative Schemes for Ab Initio Total-Energy Calculations Using a Plane-Wave Basis Set. *Phys. Rev. B* **1996**, *54*, 11169.
(35) Kresse, G.; Furthmüller, J. Efficiency of Ab-Initio Total Energy Calculations for Metals and Semiconductors Using a Plane-Wave Basis Set. *Comput. Mater. Sci.* **1996**, *6*, 15.
(36) Blöchl, P. E. Projector Augmented-Wave Method. *Phys. Rev. B* **1994**, *50*, 17953.
(37) Lazić, P. CellMatch: Combining Two-Unit Cells into a Common Supercell with Minimal Strain. *Comput. Phys. Commun.* **2015**, *197*, 324.
(38) Hamada, I. van der Waals Density Functional Made Accurate. *Phys. Rev. B* **2014**, *89*, No. 121103.
(39) Perdew, J. P.; Burke, K.; Ernzerhof, M. Generalized Gradient Approximation Made Simple. *Phys. Rev. Lett.* **1996**, *77*, 3865.
(40) Li, W. F.; Fang, C.; van Huis, M. A. Strong Spin-Orbit Splitting and Magnetism of Point Defect States in Monolayer WS_2. *Phys. Rev. B* **2016**, *94*, No. 195425.
(41) Berland, K.; Hyldgaard, P. Exchange Functional that Tests the Robustness of the Plasmon Description of the van der Waals Density Functional. *Phys. Rev.* **2014**, *89*, No. 035412.
(42) Heyd, J.; Scuseria, G. E.; Ernzerhof, M. Hybrid Functionals Based on a Screened Coulomb Potential. *J. Chem. Phys.* **2003**, *118*, 8207.
(43) Nosé, S. A molecular dynamics method for simulations in the canonical ensemble. *Mol. Phys.* **1984**, *52*, 255.
(44) Hoover, W. G. Canonical dynamics: Equilibrium phase-space distributions. *Phys. Rev. A* **1985**, *31*, 1695.
(45) Huang, H. H.; Fan, X.; Singh, D. J.; Chen, H.; Jiang, Q.; Zheng, W. T. Controlling phase transition for single-layer MTe_2 (M= Mo and W): modulation of the potential barrier under strain. *Phys. Chem. Chem. Phys.* **2016**, *18*, 4086.
(46) Rasmussen, F. A.; Thygesen, K. S. Computational 2D materials database: electronic structure of transition-metal dichalcogenides and oxides. *J. Phys. Chem. C* **2015**, *119*, 13169.
(47) Zhang, C.; Gong, C.; Nie, Y.; Min, K. A.; Liang, C.; Oh, Y. J.; Zhang, H.; Wang, W.; Hong, S.; Colombo, L.; Wallace, R. M.; et al. Systematic study of electronic structure and band alignment of monolayer transition metal dichalcogenides in Van der Waals heterostructures. *2D Mater.* **2016**, *4*, No. 015026.
(48) Zacharias, M.; Giustino, F. Theory of the special displacement method for electronic structure calculations at finite temperature. *Phys. Rev. Res.* **2020**, *2*, No. 013357.
(49) Monserrat, B.; Vanderbilt, D. Temperature dependence of the bulk Rashba splitting in the bismuth tellurohalides. *Phys. Rev. Mater.* **2017**, *1*, No. 054201.
(50) Iordanidou, K.; Persson, C. Optoelectronic properties of coexisting $InGaZnO_4$ structures. *Mater. Sci. Semicond. Process* **2021**, *121*, No. 105297.
(51) Shang, J.; Huang, L.; Wei, Z. Effects of vertical electric field and compressive strain on electronic properties of bilayer ZrS_2. *J. Semicond.* **2017**, *38*, No. 033001.

https://doi.org/10.1021/acs.chemmater.4c02738
Chem. Mater. 2024, 36, 11317−11325